



by over a hundred compounds. In fact, within the spinel space group, the fractional coordinates of the octahedral and tetrahedral sites are fixed at special positions ( $A$  on  $8a$  at  $0,0,0$ ;  $B$  on  $16d$  at  $5/8,5/8,5/8$ ), while the O atoms are on  $32e$  with coordinates  $uuu$ . This means that if the relative sizes of the  $A$  and  $B$  cations change, their positions remain the same but the oxygen array expands or contracts to accommodate them and maintain the same symmetry throughout.

The most common distortion of the spinel structure is by far the tetragonal distortion, whereby one of the cubic axes would become compressed or elongated with respect to the other two. If no additional symmetry breaking occurs, the tetragonal distortion alone decreases the symmetry from  $Fd\bar{3}m$  to  $I4_1/amd$  (No. 141). The  $c/a$  ratio is normally used as a parameter of tetragonal distortion. A phase transition from the cubic to the tetragonal structure may be induced by a sufficient concentration of non-spherical, Jahn–Teller (JT) ions, such as  $\text{Cu}^{2+}$  or  $\text{Mn}^{3+}$ , causing a cooperative distortion. Although less common, tetrahedral  $\text{Cu}^{2+}$  on the  $A$  site can display JT activity. The degeneracy of the partially occupied  $t_2$  levels is broken by compressing the tetrahedron and thereby lowering the symmetry, as in copper chromite,  $\text{CuCr}_2\text{O}_4$ , which is a tetragonally distorted spinel with unit-cell parameters ratio  $c/a < 1$  (Fig. 1, left panel).  $\text{Cu}^{2+}$  cations can be stabilized in flattened tetrahedral environments because of the preference of  $\text{Cr}^{3+}$  ions to occupy the octahedral sites. The cooperative nature of the crystal distortion can be rationalized in terms of elastic interactions among locally distorted tetrahedra, as a consequence of coupling of electronic states to bulk deformation *via* elastic strain. On heating,  $\text{CuCr}_2\text{O}_4$  undergoes a first-order structural transition from the tetragonal distorted spinel structure to the archetypal cubic spinel structure at 853 K (Yé *et al.*, 1994; Kennedy & Zhou, 2008). The structural distortion in  $\text{CuCr}_2\text{O}_4$  is large and the transition temperature high, in particular if considering that  $\text{CuO}_4$

tetrahedra are not directly linked but separated from each other by non-JT ions. Nonetheless, enhancement of the ground-state JT splitting and of lattice distortion have been explained by considering the electronic and elastic coupling of  $\text{Cu}^{2+}$  and  $\text{Cr}^{3+}$  (Atanasov *et al.*, 1993; Reinen *et al.*, 1988). The relevance of strain associated with the Jahn–Teller distortion is curiously showed in  $\text{NiCr}_2\text{O}_4$  by the observation that the crystals literally jump off a flat surface when they pass through the transition point (Crottaz *et al.*, 1997), due to the large and abrupt change in shear strain.

$\text{MgCr}_2\text{O}_4$  forms in the cubic spinel structure (Fig. 1, right panel). At room temperature (RT), the Mg-rich ( $x > 0.6$ ) members of the  $\text{Mg}_x\text{Cu}_{1-x}\text{Cr}_2\text{O}_4$  solid solution are cubic, whereas the Cu-rich members ( $x < 0.43$ ) are tetragonal. A two-phase region separates the cubic and tetragonal phases (Shoemaker & Seshadri, 2010; De *et al.*, 1983).

In this work, the effects on the crystal structure and on the tetragonal-to-cubic phase transition of progressive substitution of the Jahn–Teller and  $d^9$   $\text{Cu}^{2+}$  cation with the spherical and closed-shell  $\text{Mg}^{2+}$  cation in the  $\text{Mg}_x\text{Cu}_{1-x}\text{Cr}_2\text{O}_4$  solid solution have been studied. Given the relevance of strain in determining the structure–electronic properties relation, *in situ* high-temperature (HT) single-crystal diffraction data are analysed in terms of the evolution of symmetry-adapted strains for samples with different compositions along the joint  $\text{Mg}_x\text{Cu}_{1-x}\text{Cr}_2\text{O}_4$ . Observed variations of spontaneous strains accompanying phase transitions are expected to provide detailed insights into the transition mechanisms.

## 2. Experimental

### 2.1. Synthesis and crystal growth

Single crystals of cubic Mg-rich and tetragonal Cu-rich chromites belonging to the series  $\text{Mg}_x\text{Cu}_{1-x}\text{Cr}_2\text{O}_4$  were grown by flux decomposition methods. The synthesis of single crystals of the Mg end-member was conducted on the basis of the strategy reported by Lenaz *et al.* (2004). Starting compounds were  $\text{CuO}$  (Fluka, > 99%),  $\text{MgO}$  (Carlo Erba, > 99%) and  $\text{Cr}_2\text{O}_3$  (Merck, 99%).  $\text{Na}_2\text{B}_4\text{O}_7$  was used as a flux in a weight ratio of 2.2 with respect to the reactive mixture. The mixture was submitted to the following heating cycle: (1) heating from RT to 1473 K at a rate of  $100 \text{ K h}^{-1}$ ; (2) soaking at 1473 K for 24 h; (3) cooling to 1173 K at  $6 \text{ K h}^{-1}$ ; (4) isothermal heating at 1173 K for 9 h; (5) rapid cooling to RT. The residue was then washed with warm HCl 20%.

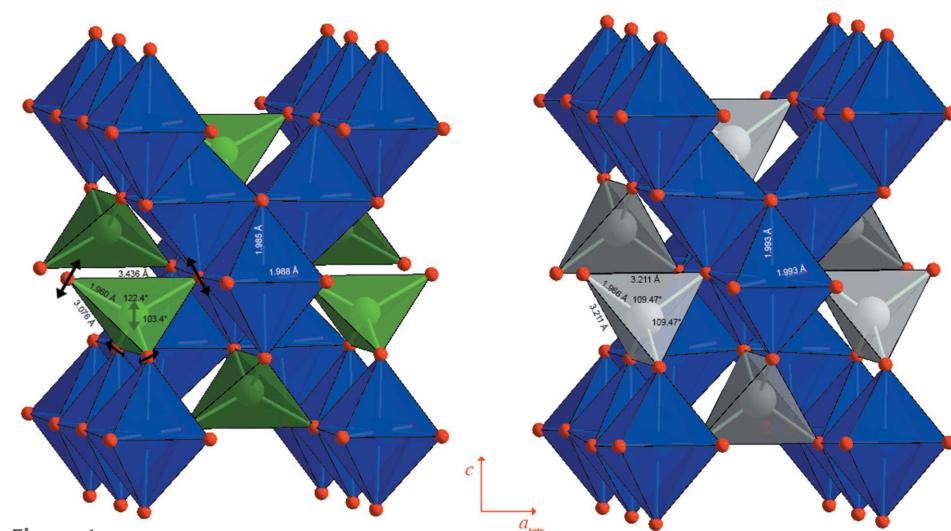


**Figure 1**  
Perspective views of the crystal structures of  $\text{CuCr}_2\text{O}_4$  (left) and  $\text{MgCr}_2\text{O}_4$  (right) along the  $a$ -axis of the  $I4_1/amd$  cell.  $\text{CuO}_4$  tetrahedra are drawn in green,  $\text{MgO}_4$  tetrahedra in grey. In  $\text{CuCr}_2\text{O}_4$ , the contraction along the  $c$  direction due to JT flattening of tetrahedral sites is given by a change of tetrahedral angles. Relevant geometrical parameters are reported.

Table 1

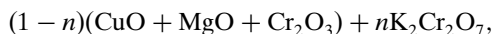
Details of data collections and structure refinements of  $\text{Mg}_x\text{Cu}_{1-x}\text{Cr}_2\text{O}_4$  crystals at RT.

Standard deviations are in parentheses and refer to the last significant digits.

	Cu100	Cu90	Cu82	Cu57	Cu47	Mg100
Crystal size (mm)	$0.5 \times 0.5 \times 0.5$	$0.2 \times 0.15 \times 0.15$	$0.2 \times 0.2 \times 0.2$	$0.15 \times 0.1 \times 0.1$	$0.1 \times 0.1 \times 0.1$	$0.15 \times 0.15 \times 0.1$
Space group	$I4_1/amd$	$I4_1/amd$	$I4_1/amd$	$I4_1/amd$	$I4_1/amd$	$Fd\bar{3}m$
$a$ (Å)	6.0287 (2)	6.0163 (1)	6.0045 (1)	5.9523 (1)	5.9435 (1)	8.3288 (1)
$c$ (Å)	7.7803 (2)	7.8279 (1)	7.8778 (1)	8.0752 (2)	8.1379 (2)	–
Reflns measured	11 427	10 608	10 480	10 314	11 374	19 474
Reflns unique	4312	4375	4372	2400†	2700†	4570
Reflns independent	295	293	294	120	128	129
Twin fraction (%)	6.6 (3)‡	14.5 (2)	13.6 (2)	27.0 (3)	22.7 (2)	–
$R_{\text{int}}$ (%)	2.40	2.04	2.41	1.65	1.93	1.78
Reflns with $I > 2\sigma_I$	3682	3791	3822	2240	2582	4480
$R_1$ (%)	2.50	2.03	2.28	4.38	2.54	1.71
$R_{\text{all}}$ (%)	2.91	2.45	2.75	4.67	2.67	1.76
$wR_2$ (%)	6.58	5.27	5.85	11.99	6.82	4.70
GOF	1.086	1.083	1.060	1.205	1.236	1.169
$\Delta\rho_{\text{max}}$ ( $\text{e } \text{Å}^{-3}$ )	0.63	0.49	0.75	0.76	0.44	0.63
$\Delta\rho_{\text{min}}$ ( $\text{e } \text{Å}^{-3}$ )	–1.14	–0.70	–1.03	–0.88	–0.59	–0.54

† Dataset limited to  $\sin \theta/\lambda = 0.7 \text{ \AA}^{-1}$ . ‡ Three twin components with relative abundances of second and third components 3.7 (3), 2.9 (3).

$\text{Mg}_x\text{Cu}_{1-x}\text{Cr}_2\text{O}_4$  solid solution, the method reported by Yé *et al.* (1994) for growing crystals of  $\text{CuCr}_2\text{O}_4$  has been adapted to different Cu/Mg stoichiometric ratios. Starting compounds were CuO (Fluka, > 99%), MgO (Carlo Erba, > 99%) and  $\text{K}_2\text{Cr}_2\text{O}_7$  (Carlo Erba, > 99%).  $\text{K}_2\text{Cr}_2\text{O}_7$  transforms into  $\text{Cr}_2\text{O}_3$ , which, when freshly formed, is highly reactive towards copper oxide. Potassium dichromate acts as a reactive flux for the crystal growth and an excess amount was therefore added according to



where  $n$  was chosen to be equal to 0.2 mol.  $\text{B}_2\text{O}_3$  (1 wt%) was added to the mixture in order to increase the homogeneity of the solution and hence improve the quality of the crystals. Different CuO/MgO stoichiometric ratios were used to obtain spinels with nominal compositions:  $\text{CuCr}_2\text{O}_4$  ( $x = 0$ ),  $\text{Mg}_{0.05}\text{Cu}_{0.95}\text{Cr}_2\text{O}_4$  ( $x = 0.05$ ),  $\text{Mg}_{0.1}\text{Cu}_{0.9}\text{Cr}_2\text{O}_4$  ( $x = 0.1$ ),  $\text{Mg}_{0.4}\text{Cu}_{0.6}\text{Cr}_2\text{O}_4$  ( $x = 0.4$ ). The mixtures were submitted to the following heating cycle: (1) heating from RT to 1093 K at  $100 \text{ K h}^{-1}$ ; (2) soaking at 1093 K for 24 h; (3) cooling at  $30 \text{ K h}^{-1}$ . Given the high refractory properties of MgO, stage (2) was prolonged for 115 h in the case of the mixture with  $x = 0.4$ . After the thermal runs, the residues were washed with boiling water and the single crystals removed from the solidified flux.

## 2.2. Single-crystal XRD at room temperature

Several crystals were isolated from each synthesis residue. They were checked for crystal quality by analysing X-ray diffraction profiles. The selected crystals, labelled Cu100, Cu90, Cu82, Cu57, Cu47 and Mg100 on the basis of their actual compositions as determined from structure refinements and electron-microprobe analyses (see §§2.4 and 2.5), were submitted to single-crystal diffraction analysis at RT using a Bruker-AXS APEX diffractometer equipped with a CCD detector. Data collections were carried out with operating

conditions 50 kV and 30 mA and graphite-monochromated Mo  $K\alpha$  radiation ( $\lambda = 0.7107 \text{ \AA}$ ). The Bruker SMART system of programs was used for preliminary crystal lattice determination and X-ray data collection. A total of 4800 frames (resolution:  $512 \times 512$  pixels) were collected with eight different goniometer settings using the  $\omega$ -scan mode (scan width:  $0.3^\circ\omega$ ; exposure time: 5–20 s per frame, depending on the size and relative scattering power of the crystals analysed; detector–sample distance: 60 mm). Complete data collection was achieved up to  $\sin \theta/\lambda$  ca  $0.95 \text{ \AA}^{-1}$ .

All the tetragonal crystals of the series were twinned, as expected given the synthesis conditions which imply the use of high temperature, where the cubic phase is stable, and subsequent transformation to tetragonal on cooling.  $I4_1/amd$  is a maximal nonisomorphic  $t$ -subgroup of  $Fd\bar{3}m$  and the formation of ferroelastic domains, including transformation twinning, is inevitable during the phase transition. The corresponding ferroelastic species according to Aizu's notation (Aizu, 1969) is  $m\bar{3}mF4/mmm$ , where 'F' stands for ferroic, and separates the parent point group ( $m\bar{3}m$ ) from the derived point group ( $4/mmm$ ). As  $m\bar{3}m$  and  $4/mmm$  are of the order 48 and 16, respectively, there are three possible orientation states in the tetragonal phase. In our study, three twin components were found to be present in crystal Cu100, while two components were detected in the other tetragonal crystals.

The Bruker program SAINT+ was used for the data reduction, including intensity integration, background and Lorentz–polarization corrections. Intensity data from the twin components present in tetragonal crystals were integrated taking into account the superposition affecting some diffraction spots. Final unit-cell parameters were obtained by the Bruker GLOBAL least-squares orientation matrix refinement procedure, based on the positions of all measured reflections. The semi-empirical absorption correction of Blessing (1995), based on the determination of transmission factors for equivalent reflections, was applied using the Bruker programs SADABS or, for twinned crystals, TWINABS (Sheldrick,

**Table 2**

Tetragonal unit-cell parameters of  $\text{Mg}_x\text{Cu}_{1-x}\text{Cr}_2\text{O}_4$  crystals at different temperatures.

Standard deviations are in parentheses and refer to the last significant digits.

<i>T</i> (K)	Cu100		Cu90		Cu82		<i>T</i> (K)	Cu54†	
	<i>a</i> (Å) × √2	<i>c</i> (Å)	<i>a</i> (Å) × √2	<i>c</i> (Å)	<i>a</i> (Å) × √2	<i>c</i> (Å)		<i>a</i> (Å) × √2	<i>c</i> (Å)
298	8.5249 (6)	7.7811 (10)	8.5103 (5)	7.8320 (11)	8.4924 (7)	7.8771 (10)	298	8.401 (3)	8.122 (4)
323	8.5264 (6)	7.7826 (10)	8.5128 (4)	7.8335 (6)	8.4914 (6)	7.8810 (8)	323	8.402 (2)	8.140 (2)
348	8.5257 (5)	7.7900 (8)	8.5124 (5)	7.8409 (5)	8.4900 (6)	7.8889 (8)	343	8.397 (2)	8.162 (3)
373	8.5251 (4)	7.7962 (7)	8.5118 (5)	7.8488 (7)	8.4913 (6)	7.8970 (7)	353	8.391 (4)	8.177 (6)
398	8.5252 (4)	7.8026 (7)	8.5117 (5)	7.8564 (5)	8.4899 (6)	7.9053 (7)	363	8.388 (2)	8.204 (4)
423	8.5253 (4)	7.8092 (8)	8.5105 (5)	7.8644 (7)	8.4890 (5)	7.9147 (5)	373	8.385 (3)	8.220 (4)
448	8.5257 (4)	7.8149 (8)	8.5102 (5)	7.8724 (7)	8.4880 (6)	7.9233 (6)	383	8.380 (5)	8.242 (9)
473	8.5249 (6)	7.8222 (9)	8.5094 (5)	7.8804 (5)	8.4849 (6)	7.9340 (8)	393	8.369 (5)	8.276 (9)
498	8.5253 (5)	7.8286 (10)	8.5081 (5)	7.8897 (6)	8.4843 (6)	7.9457 (6)	403	8.362 (4)	8.288 (7)
523	8.5239 (4)	7.8350 (7)	8.5089 (7)	7.8989 (9)	8.4826 (6)	7.9581 (5)	413	8.350 (3)	8.306 (6)
548	8.5237 (5)	7.8444 (9)	8.5058 (5)	7.9093 (6)	8.4789 (7)	7.9716 (7)	423	8.344 (2)	8.320 (3)
573	8.5229 (4)	7.8529 (7)	8.5046 (8)	7.9198 (9)	8.4750 (7)	7.9880 (6)	423‡	8.338 (3)	8.320 (6)
598	8.5224 (5)	7.8610 (8)	8.5016 (6)	7.9320 (8)	8.4699 (11)	8.0072 (15)	–	–	–
623	8.5215 (5)	7.8706 (8)	8.4981 (8)	7.9467 (9)	8.4590 (10)	8.0337 (15)	–	–	–
648	8.5188 (5)	7.8813 (8)	8.4940 (8)	7.9620 (11)	–	–	–	–	–
673	8.5182 (4)	7.8921 (7)	8.4892 (12)	7.9811 (20)	–	–	–	–	–
698	8.5155 (5)	7.9043 (8)	–	–	–	–	–	–	–
723	8.5129 (5)	7.9169 (9)	–	–	–	–	–	–	–
748	8.5095 (5)	7.9337 (9)	–	–	–	–	–	–	–
773	8.5055 (4)	7.9479 (8)	–	–	–	–	–	–	–
788	8.4998 (4)	7.9655 (7)	–	–	–	–	–	–	–
803	8.4955 (5)	7.9793 (8)	–	–	–	–	–	–	–
818	8.4899 (5)	7.9964 (7)	–	–	–	–	–	–	–

† Crystal size: 0.15 × 0.15 × 0.15 mm. ‡ On cooling.

2003). Details of room-temperature data collection by the CCD diffractometer are reported in Table 1.

### 2.3. Single-crystal XRD at high temperature

Crystals Cu100, Cu90, Cu82, Cu54 (not measured at RT by the CCD diffractometer) and Mg100 were submitted to *in situ* high-temperature single-crystal diffraction investigations using a Philips PW1100 four-circle diffractometer with point-counter detector. Crystals Cu57 and Cu47 were not used for the HT study due to their low diffracted intensities. Operating conditions were 55 kV and 30 mA with graphite-mo-chromated Mo *K*α radiation ( $\lambda = 0.7107 \text{ \AA}$ ). Horizontal and vertical apertures of the point counter detector were 2.0 and 1.5°, respectively. High-temperature measurements were performed by using a home-made U-shaped microfurnace, which has been in use in our laboratory for over 15 years. It makes use of a Pt–Pt/Rh resistance, which allows temperatures up to 1273 K to be achieved, and is equipped with a K-type thermocouple. Temperature calibration (calibration curve  $R^2 = 0.9994$ ) is regularly done by known melting points of several pure compounds and by the transition temperature of quartz (Carpenter, Salje, Graeme-Barber, Wruck *et al.*, 1998). Reported temperatures are precise to within ±5 K in the whole temperature range. The design of the furnace limits the angular excursion of the  $\omega$  circle to *ca* 27.5° ( $\sin \theta/\lambda$  *ca* 0.65 Å<sup>-1</sup> with Mo *K*α radiation). As routinely done for HT measurements using this system, the selected crystals were inserted into quartz capillaries (0.3–0.5 mm Ø, depending on the dimensions of the crystals) and kept in position by means of quartz wool in order to avoid any mechanical stress. Unit-

**Table 3**

Cubic unit-cell parameters of  $\text{Mg}_x\text{Cu}_{1-x}\text{Cr}_2\text{O}_4$  crystals at different temperatures.

Standard deviations are in parentheses and refer to the last significant digits. Some intermediate data have been omitted in the table but are present in the graphs.

<i>T</i> (K)	Cu100	Cu90	Cu82	Cu54	Mg100
298	–	–	–	–	8.3312 (4)
323	–	–	–	–	8.3304 (4)
373	–	–	–	–	8.3342 (4)
423	–	–	–	–	8.3369 (3)
433	–	–	–	8.337 (4)	–
473	–	–	–	8.337 (2)	8.3391 (4)
523	–	–	–	8.339 (2)	8.3420 (5)
573	–	–	–	8.340 (2)	8.3458 (4)
623	–	–	–	8.347 (2)	8.3491 (5)
673	–	–	–	8.348 (2)	8.3523 (4)
698	–	–	8.3314 (5)	–	–
723	–	–	8.3333 (5)	8.353 (2)	8.3557 (5)
773	–	8.3393 (6)	8.3372 (5)	8.356 (2)	8.3571 (5)
823	–	8.3424 (6)	8.3420 (4)	8.358 (2)	8.3616 (5)
873	8.3411 (5)†	8.3448 (6)	8.3446 (4)	8.359 (2)	8.3635 (5)
898	8.3431 (4)	8.3466 (6)	–	–	–
923	8.3465 (7)	8.3492 (5)	8.3502 (5)	8.363 (2)	8.3686 (5)
973	8.3505 (9)	8.3523 (6)	8.3498 (5)	8.366 (2)	8.3711 (5)
1023	8.3546 (11)	8.3564 (6)	8.3545 (5)	8.369 (2)	8.3734 (5)
1073	8.3557 (7)	8.3601 (6)	8.3572 (4)	8.372 (2)	8.3769 (5)
1123	8.3609 (6)	–	8.3626 (5)	8.374 (2)	8.3797 (5)
1173	8.3622 (4)	8.3667 (6)	8.3665 (5)	8.378 (2)	8.3828 (6)

† Measured at 863 K.

cell parameters were measured from RT up to 1173 K at regular steps. At each working temperature, the orientation matrix was updated by centring 24 reflections selected in the range of  $\sin \theta/\lambda$  *ca* 0.2–0.34 Å<sup>-1</sup>, and accurate lattice param-

**Table 4**  
Details on data collections and structure refinements of  $\text{Mg}_x\text{Cu}_{1-x}\text{Cr}_2\text{O}_4$  crystals at HT.

	Reflns measured	Reflns independent	$R_{\text{int}}$ (%)	Reflns $I > 2\sigma_I$	$R_1$ (%)	$R_{\text{all}}$ (%)	$wR_2$ (%)	GOF	$\Delta\rho_{\text{max}}$ ( $\text{e \AA}^{-3}$ )	$\Delta\rho_{\text{min}}$ ( $\text{e \AA}^{-3}$ )
<b>Cu100</b>										
298 K	187	89	3.31	76	2.11	2.76	5.41	1.143	0.41	-0.77
373 K	187	89	3.73	77	2.71	3.12	5.71	1.111	0.59	-1.15
473 K	191	91	3.57	79	2.72	3.19	5.93	1.060	0.53	-1.21
573 K	191	91	3.04	78	2.72	3.40	7.01	1.158	0.56	-1.06
673 K	192	92	3.41	78	2.71	3.30	6.10	1.175	0.64	-1.03
773 K	195	93	2.74	78	2.61	3.49	6.21	1.112	0.45	-0.87
803 K	195	93	2.59	78	2.74	3.54	6.84	1.142	0.64	-1.00
863 K	192	45†	5.32	41	3.34	3.72	7.47	1.329	0.91	-0.53
973 K	192	45†	11.49	37	7.05	7.68	10.50	1.422	3.25	-1.01
1073 K	192	45†	19.08	38	8.42	9.26	12.44	1.190	3.70	-0.86
<b>Cu90</b>										
298 K	191	91	1.54	78	1.87	2.62	4.86	1.114	0.51	-0.69
373 K	191	91	2.25	75	2.23	3.16	5.84	1.171	0.60	-0.91
473 K	191	91	2.21	74	2.53	3.43	6.70	1.152	0.54	-0.92
573 K	193	92	2.73	74	2.42	3.45	6.15	1.127	0.50	-0.94
673 K	196	93	2.83	79	3.08	3.77	6.84	1.138	0.63	-1.16
773 K	192	45†	2.13	37	1.44	2.14	3.41	1.247	0.34	-0.33
873 K	192	45†	2.41	36	1.66	2.45	5.41	1.432	0.46	-0.48
973 K	192	45†	2.58	38	1.73	2.35	5.17	1.253	0.34	-0.42
1073 K	192	45†	2.55	38	1.67	2.65	5.04	1.230	0.43	-0.44
1173 K	192	45†	2.67	38	1.82	3.09	5.68	1.304	0.67	-0.61
<b>Cu82</b>										
298 K	191	91	2.20	76	3.59	4.16	9.15	1.219	0.65	-1.59
373 K	193	92	2.85	76	3.48	4.61	8.53	1.167	0.70	-1.64
473 K	387	93	3.02	76	3.22	4.36	8.39	1.064	0.89	-1.31
573 K	196	93	3.44	80	3.89	4.53	9.25	1.147	0.71	-1.47
623 K	388	93	3.90	76	3.50	4.36	8.64	1.186	0.82	-1.55
673 K	192	45†	14.20	37	6.65	7.96	12.92	1.090	3.03	-1.80
723 K	192	45†	2.02	37	1.41	2.11	5.24	1.248	0.39	-0.29
823 K	756	45†	2.16	38	1.68	2.43	4.90	1.199	0.34	-0.33
923 K	192	45†	2.14	38	1.59	2.40	4.88	1.312	0.26	-0.30
1023 K	192	45†	2.54	38	1.67	2.47	5.39	1.298	0.42	-0.30
<b>Cu54</b>										
298 K	196	93	6.50	78	4.56	5.49	10.00	1.115	0.85	-0.80
353 K	197	94	11.09	74	4.83	6.00	11.79	1.121	0.98	-0.75
473 K	728	45†	2.47	41	2.93	3.25	6.51	1.134	0.62	-0.62
673 K	192	45†	2.90	40	3.41	3.76	7.62	1.105	0.52	-0.79
873 K	192	45†	3.04	41	3.59	3.79	8.33	1.186	0.47	-0.83
1073 K	192	45†	2.97	40	3.35	3.89	7.26	1.210	0.61	-0.77
423 K‡	201	96	2.51	85	2.31	2.85	6.22	1.114	0.48	-0.47
<b>Mg100</b>										
298 K	192	45†	1.94	43	2.25	2.27	8.32	1.351	0.44	-0.48
523 K	192	45†	2.11	39	2.01	3.00	5.53	1.333	0.62	-0.41
973 K	756	45†	2.77	39	2.43	3.38	6.04	1.217	0.69	-0.48

† Cubic. ‡ On cooling

eters (reported in Tables 2 and 3 for tetragonal and cubic phases, respectively) were derived from a least-squares procedure based on the Philips LAT routine over up to 60  $d^*$ -spacings, each measured from the positions of all reflection pairs at  $\pm\theta$  in the range of  $\sin \theta/\lambda$  0.073–0.628  $\text{\AA}^{-1}$ .

For each crystal, complete datasets of diffracted intensities were collected at different temperatures, both below and above the phase transition temperature, using the same operating conditions as reported above. Intensity data were measured in the  $\sin \theta/\lambda$  range 0.05–0.628  $\text{\AA}^{-1}$  in the  $\omega$ -scan mode ( $2.0^\circ$   $\theta$  scan width;  $0.05^\circ$   $\theta$   $\text{s}^{-1}$  scan speed). Only diffraction spots belonging to the orientation matrix of the

main twin component were measured, thus including overlapping reflections. Three standard reflections were collected every 200 measured reflections. X-ray diffraction intensities were obtained by measuring step-scan profiles and analysing them by the Lehmann & Larsen (1974)  $\sigma_p/I$  method, as modified by Blessing *et al.* (1974). Intensities were corrected for absorption using the semi-empirical  $\varphi$ -scan method of North *et al.* (1968). Relevant parameters for data collected at different temperatures are reported in Table 4. Some reflections, representative of different classes, were also scanned periodically ( $\omega/2\theta$  scan mode;  $2.0^\circ$   $\theta$  scan width;  $0.1^\circ$   $\theta$   $\text{s}^{-1}$  scan speed) to check for the crystallinity of the sample.

**Table 5**

Electron microprobe analyses and selected geometrical parameters for  $\text{Mg}_x\text{Cu}_{1-x}\text{Cr}_2\text{O}_4$  crystals at RT.

Standard deviations are in parentheses and refer to the last significant digits. OAV = Octahedral Angle Variance; OQE = Octahedral Quadratic Elongation; TAV = Tetrahedral Angle Variance; TQE = Tetrahedral Quadratic Elongation (Robinson *et al.*, 1971).

	Cu100	Cu90	Cu82	Cu57	Cu47	Mg100
$x$ (site occupancy)	0	0.103 (1)	0.183 (1)	0.442 (5)	0.504 (2)	1
$x$ (EPMA) <sup>†</sup>	0 (0)	0.103 (21)	0.178 (28)	0.428 (41)	0.527 (7)	–
$a\sqrt{2}/c$	1.0958 (3)	1.0869 (2)	1.0779 (2)	1.0424 (3)	1.0328 (3)	1
$V_{\text{octahedron}}$ ( $\text{\AA}^3$ )	10.31	10.30	10.30	10.33	10.37	10.41
Cr–O <sub>axial</sub> ( $\text{\AA}$ ) $\times 2$	1.9854 (5)	1.9852 (4)	1.9865 (4)	1.9807 (13)	1.9872 (6)	1.9927 (1)
Cr–O <sub>equatorial</sub> ( $\text{\AA}$ ) $\times 4$	1.9884 (3)	1.9875 (2)	1.9870 (3)	1.9911 (9)	1.9915 (4)	1.9927 (1)
Cr–O <sub>average</sub> ( $\text{\AA}$ )	1.9874 (3)	1.9867 (2)	1.9869 (2)	1.9876 (7)	1.9990 (4)	1.9927 (1)
OAV ( $^\circ$ )	37.26	36.99	36.56	34.11	34.10	33.35
OQE	1.0101	1.0100	1.0099	1.0091	1.0091	1.0088
Cr–Cr ( $\text{\AA}$ )	2.8856 (1)	2.8904 (1)	2.8958 (1)	2.9162 (1)	2.9248 (1)	2.9447 (1)
$V_{\text{tetrahedron}}$ ( $\text{\AA}^3$ )	3.71	3.74	3.77	3.85	3.87	3.90
(Cu,Mg)–O ( $\text{\AA}$ )	1.9598 (4)	1.9607 (4)	1.9615 (4)	1.9616 (12)	1.9646 (6)	1.9660 (3)
O–(Cu,Mg)–O ( $^\circ$ ) $\times 2$	103.40 (1)	103.89 (1)	104.39 (1)	106.80 (4)	107.29 (2)	109.47
O–(Cu,Mg)–O ( $^\circ$ ) $\times 4$	122.45 (3)	121.31 (2)	120.21 (3)	114.97 (8)	113.92 (4)	109.47
O...O edge ( $\text{\AA}$ ) $\times 2$	3.0760 (5)	3.0879 (4)	3.0994 (5)	3.150 (2)	3.1644 (6)	3.2106 (2)
O...O edge ( $\text{\AA}$ ) $\times 4$	3.4355 (6)	3.4183 (5)	3.4009 (6)	3.308 (2)	3.2938 (8)	3.2106 (2)
TAV ( $^\circ$ )	96.86	80.96	66.78	17.81	11.72	0
TQE	1.0270	1.0223	1.0182	1.0047	1.0031	1.0000

<sup>†</sup> EPMA for sample Cu54 gave  $x = 0.460$  (71).

### 2.4. Structure refinements

All structure refinements were carried out by full-matrix least-squares using *SHELXL97* (Sheldrick, 2008). Equivalent reflections were averaged, and the resulting internal agreement factors  $R_{\text{int}}$  are reported in Table 1 for all the datasets collected at RT, and in Table 4 for datasets collected at HT. The atomic scattering curves were taken from *International Tables for X-ray Crystallography* (Ibers & Hamilton, 1974). For datasets collected at RT by the CCD diffractometer, contributions from the different twin components were taken into account by using the HKLF-5 format in *SHELXL97* and

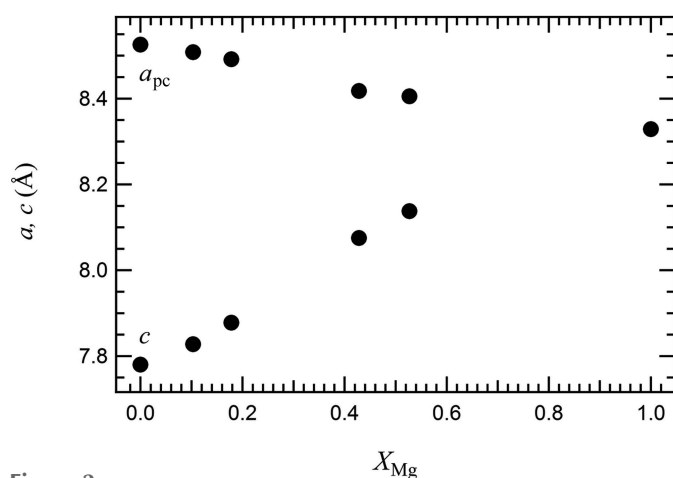


**Figure 2**

Variation of unit-cell parameters as a function of composition at room temperature across the  $\text{Mg}_x\text{Cu}_{1-x}\text{Cr}_2\text{O}_4$  join. For ease of comparison, the  $a$  parameter in the low-temperature tetragonal phase has been scaled and displayed in the pseudocubic setting  $a_{\text{pc}} = a\sqrt{2}$ . The vertical size of the symbols exceeds the uncertainties in unit-cell parameters.

including the BASF parameter in the refinement. For all structure refinements, structure factors were weighted according to  $w = 1/[\sigma^2(F_o^2) + (AP)^2 + BP]$ , where  $P = (F_o^2 + 2F_c^2)/3$ , and  $A$  and  $B$  were chosen for every crystal to produce a flat analysis of variance in terms of  $F_c^2$ , as suggested by the program. An extinction parameter  $x$  was refined to correct the structure factors according to the equation:  $F_o = F_c k [1 + 0.001x F_c^2 \lambda_3 / \sin 2\theta]^{-1/4}$  (where  $k$  is the overall scale factor). In addition to  $x$  and  $k$ , atomic positions, anisotropic displacement parameters and site occupancy at the  $A$  site (for terms with intermediate composition) were refined simultaneously. The Cu/Mg ratios obtained from unconstrained refinements of site occupancy were close to the nominal compositions and were then confirmed by electron microprobe analyses performed on the same crystals at the end of the HT

experiments (see §2.5). Final difference-Fourier maps were featureless. Values of the conventional agreement indices,  $R_1$  and  $R_{\text{all}}$ , as well as the goodness of fit ( $S$ ) are reported in Tables 1 and 4 for RT and HT datasets, respectively, whereas interatomic distances and selected geometrical parameters are reported in Table 5 for the RT datasets and in Tables 6–10 for the HT datasets. Atomic fractional coordinates, anisotropic displacement parameters  $U_{ij}$  and lists of observed and calculated structure factors are available in the CIF files of supporting information.

### 2.5. Electron probe microanalyses (EPMA)

At the end of the diffraction experiments, all the crystals used in the present study were embedded in epoxy resin, polished and analysed by electron microprobe. The chemical compositions were measured with a Jeol JXA-8200 electron microprobe, fully automated with 5 crystals and 5 wavelength dispersive spectrometers. The polished samples were coated with about 10 nm of amorphous carbon to avoid charging of the surface and studied at acceleration voltages of 15 kV and probe current of 15 nA. The analytical standards used for the calibration of the energy position of the analyzed elements were  $\text{Cu}_2\text{O}$ ,  $\text{MgO}$  and  $\text{Cr}_2\text{O}_3$  for Cu, Mg and Cr, respectively. For each sample, 10 to 15 points were measured and the averaged chemical compositions, as well as the corresponding standard deviations, are reported in Table 5.

## 3. Results and discussion

### 3.1. Unit-cell parameters and geometry of tetrahedra at RT

Refinements of X-ray diffraction data reveal a high sensitivity of the crystal structure to the amount of  $\text{Cu}^{2+}$  present.

Table 6

Selected geometrical parameters for  $\text{CuCr}_2\text{O}_4$  (Cu100) at HT.

Standard deviations are in parentheses and refer to the last significant digits. OAV = Octahedral Angle Variance; OQE = Octahedral Quadratic Elongation; TAV = Tetrahedral Angle Variance; TOE = Tetrahedral Quadratic Elongation (Robinson *et al.*, 1971).

	298 K	373 K	473 K	573 K	673 K	773 K	803 K	863 K	973 K	1073 K
$V_{\text{oct}} (\text{\AA}^3)$	10.30	10.30	10.33	10.38	10.39	10.33	10.38	10.38	10.25	10.26
$\text{Cr}-\text{O}_{\text{axial}} (\text{\AA}) \times 2$	1.985 (5)	1.983 (5)	1.991 (4)	1.992 (5)	1.991 (5)	1.986 (4)	1.997 (5)	1.992 (4)	1.988 (9)	1.986 (4)
$\text{Cr}-\text{O}_{\text{eq}} (\text{\AA}) \times 4$	1.988 (2)	1.989 (2)	1.988 (2)	1.992 (3)	1.993 (2)	1.990 (2)	1.990 (3)	1.992 (4)	1.985 (4)	1.986 (4)
$\text{Cr}-\text{O}_{\text{av}} (\text{\AA})$	1.987 (3)	1.987 (3)	1.989 (3)	1.992 (4)	1.992 (3)	1.989 (3)	1.992 (4)	1.992 (4)	1.985 (4)	1.986 (4)
OAV ( $^\circ$ )	37.42	37.71	38.18	36.36	36.69	39.83	38.00	36.60	44.97	45.38
OQE	1.0102	1.0102	1.0103	1.0098	1.0099	1.0107	1.0102	1.0097	1.0118	1.0120
$\text{Cr}-\text{Cr} (\text{\AA})$	2.8855 (2)	2.8881 (1)	2.8925 (2)	2.8973 (1)	2.9031 (1)	2.9102 (2)	2.9138 (2)	2.9490 (2)	2.9523 (3)	2.9542 (2)
$V_{\text{tet.}} (\text{\AA}^3)$	3.71	3.74	3.75	3.76	3.80	3.88	3.87	3.96	4.08	4.09
$\text{Cu}-\text{O} (\text{\AA})$	1.960 (4)	1.962 (4)	1.965 (4)	1.963 (5)	1.967 (4)	1.977 (4)	1.974 (4)	1.976 (7)	1.996 (7)	1.998 (8)
$\text{O}-\text{Cu}-\text{O} (^\circ) \times 2$	103.4 (1)	103.6 (1)	103.6 (1)	103.9 (1)	104.3 (1)	105.0 (1)	105.0 (1)	109.47	109.47	109.47
$\text{O}-\text{Cu}-\text{O} (^\circ) \times 4$	122.4 (3)	122.0 (3)	121.9 (2)	121.2 (3)	120.3 (3)	118.9 (2)	118.8 (3)	109.47	109.47	109.47
$\text{O}\cdots\text{O}$ edge ( $\text{\AA}) \times 2$	3.077	3.084	3.089	3.093	3.107	3.136	3.132	3.226	3.253	3.252
$\text{O}\cdots\text{O}$ edge ( $\text{\AA}) \times 4$	3.435	3.432	3.436	3.422	3.413	3.406	3.397	3.226	3.253	3.252
TAV ( $^\circ$ )	96.52	90.18	89.22	80.05	68.37	52.10	50.37	0	0	0
TOE	1.027	1.0250	1.0247	1.0221	1.0187	1.0141	1.0136	1.0000	1.0000	1.0000

The unit-cell parameters are reported as a function of Mg content in Fig. 2. They are expressed in terms of the cubic unit cell itself ( $\text{MgCr}_2\text{O}_4$ ) or of the reduced pseudocubic cell ( $I4_1/amd$  structures of the Cu-rich samples). Samples with  $x \leq 0.53$  are isostructural with  $\text{CuCr}_2\text{O}_4$ , thus the tetragonal region seems slightly larger than previously reported by De *et al.* (1983), in agreement with recent data of Shoemaker &

Seshadri (2010). Across the solid solution, starting from tetragonal  $\text{CuCr}_2\text{O}_4$ , replacement of Cu by Mg is accompanied by an increase in the  $c$ -axis and a decrease in the  $a$ -axis lengths, and hence leads to a gradual decrease of the tetragonal distortion.

The influence of the Jahn–Teller effect can be better estimated by looking at the geometry of the tetrahedra. These are flattened and, with respect to the ideal tetrahedron, display four smaller and two angles larger than  $109.47^\circ$  (see Fig. 1 for visual reference). The distortion of the tetrahedra is large, with  $\Delta\text{O}-\text{Cu}-\text{O} = 12.94^\circ$  in the Cu end-member. The distortion of the tetrahedra in the tetragonal phase is also evident in the behaviour of the  $\text{O}\cdots\text{O}$  edges. In Fig. 3,  $\text{O}-(\text{Cu},\text{Mg})-\text{O}$  angles and  $\text{O}\cdots\text{O}$  edges are plotted as a function of composition. With increasing Mg content, the flattening of the tetrahedra is reduced: the two sets of  $\text{O}-(\text{Cu},\text{Mg})-\text{O}$  tetrahedral angles converge towards  $109.47^\circ$ , as required by the  $4\bar{3}m$  site symmetry of the cubic phase. A similar behaviour is shown by the tetrahedral edges. Variation of the  $(\text{Cu},\text{Mg})-\text{O}$  bond length (Table 5) is related to the difference in ion size between  $\text{Cu}^{2+}$  and  $\text{Mg}^{2+}$ .

Homogeneity of the solid solution is quite good. EPMA spot analyses reveal a rather narrow composition range within each sample (Table 5), with Cu54 and Cu47 showing the highest e.s.d.s. When looking at the equivalent atomic displacement parameters (ADPs; Fig. 4a), crystals with intermediate compositions show slightly higher values than those of the two end-members due to some static disorder, with an overall behaviour that is common for solid solutions. Interestingly and as already reported previously (*e.g.* Kennedy & Zhou, 2008), in all Cu-bearing crystals, the Cu/Mg site is the one showing the highest displacement parameters. This is mainly due to an elongated displacement ellipsoid towards the  $c$ -axis (Fig. 4b). The  $R_{\text{max}}/R_{\text{min}}$  ratio of the principal axes of the thermal ellipsoid is 2.67 for the tetrahedral cation in Cu100 and decreases almost linearly with increasing Mg content, with Cu47 slightly deviating from this trend likely due to some compositional heterogeneity. However, the behaviour

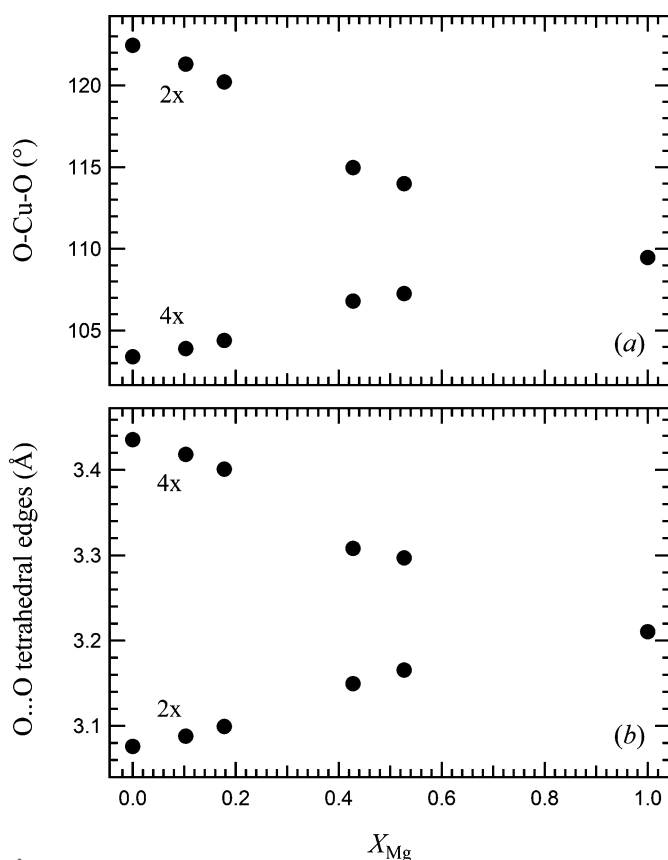
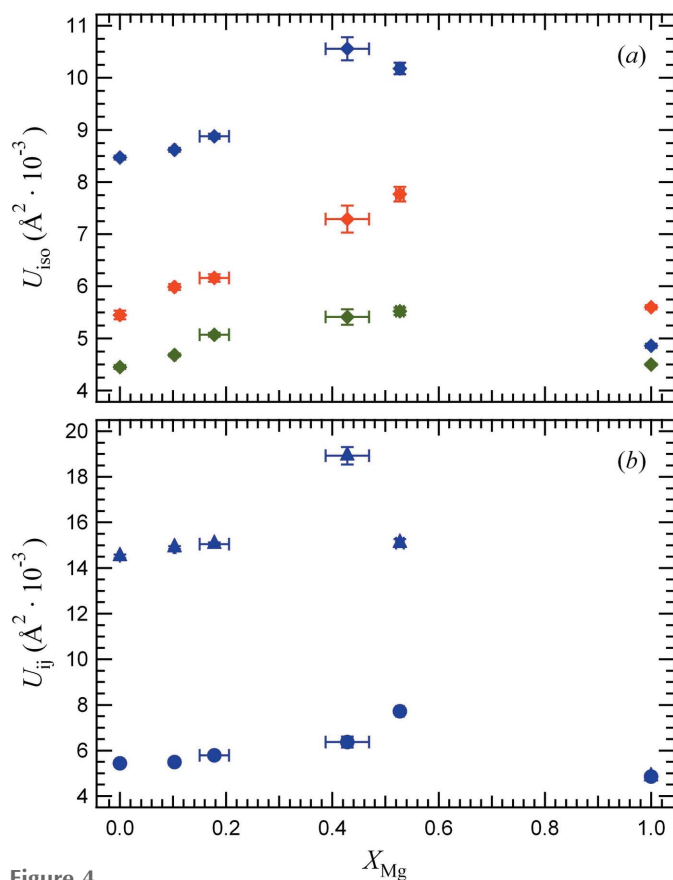
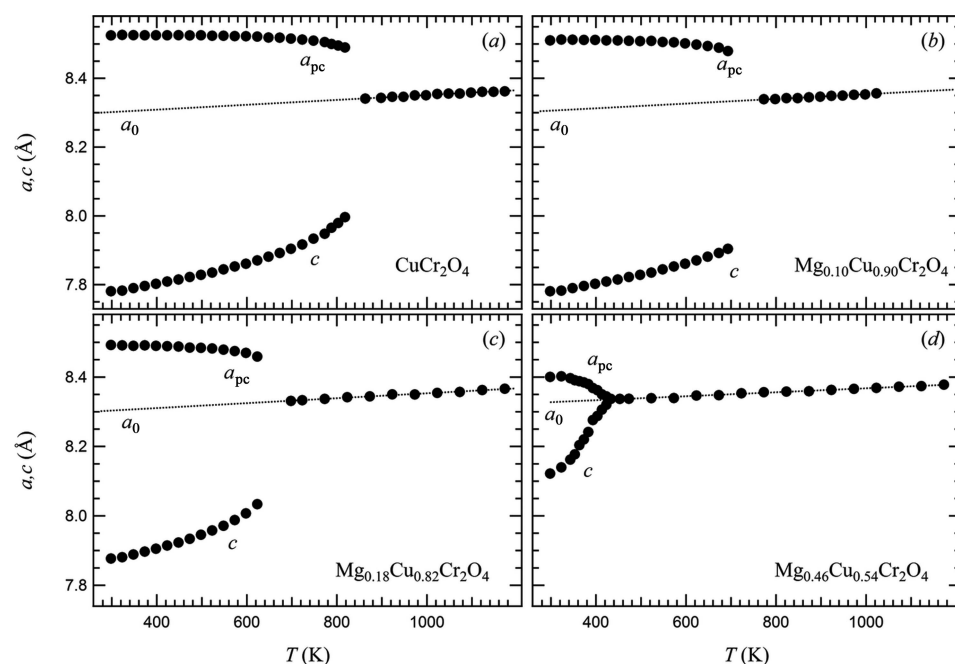


Figure 3

Variation of (a) tetrahedral  $\text{O}-(\text{Cu},\text{Mg})-\text{O}$  angles and (b)  $\text{O}\cdots\text{O}$  edges as a function of Mg content. Error bars are within the symbols.



**Figure 4**  
Variation of atomic displacement parameters as a function of composition: (a) isotropic ADPs of Cu/Mg (blue diamonds), Cr (green diamonds) and O (red diamonds); (b) anisotropic ADPs  $U_{11}$  (circles) and  $U_{33}$  (triangles) for the Cu/Mg site.



**Figure 5**  
Variation as a function of temperature of unit-cell parameters for spinel samples of different compositions across the  $\text{Mg}_x\text{Cu}_{1-x}\text{Cr}_2\text{O}_4$  join. (a)  $\text{CuCr}_2\text{O}_4$ ; (b)  $\text{Mg}_{0.10}\text{Cu}_{0.90}\text{Cr}_2\text{O}_4$ ; (c)  $\text{Mg}_{0.18}\text{Cu}_{0.82}\text{Cr}_2\text{O}_4$ ; (d)  $\text{Mg}_{0.46}\text{Cu}_{0.54}\text{Cr}_2\text{O}_4$ . The values of  $a_0$  are the lattice parameters of the respective cubic parent phase extrapolated from high temperature into the stability field of the tetragonal phase.

observed for the average structure by XRD does not necessarily allow to differentiate the distinct cation coordinations of  $\text{Mg}^{2+}$  and  $\text{Cu}^{2+}$  if they are different on the local length scale.

### 3.2. High-temperature behaviour

The temperature dependence of the lattice parameters for  $\text{CuCr}_2\text{O}_4$  and all the intermediate compounds of the series  $\text{Mg}_x\text{Cu}_{1-x}\text{Cr}_2\text{O}_4$  is shown in Fig. 5. Heating the samples results in a gradual reduction of the splitting of  $a$  and  $c$  unit-cell parameters. Variation of the unit-cell parameters with temperature for  $\text{CuCr}_2\text{O}_4$  is in good agreement with previously reported data (Kennedy & Zhou, 2008) and shows (Fig. 5a) a large first-order jump above 818 K, when the tetragonal splitting is abruptly lost. By inspection of the variations of the lattice parameters for the samples of intermediate compositions (Figs. 5b–d), it is possible to note how the gradual substitution of Cu for Mg causes a reduction of the initial  $a$ – $c$  splitting and of the discontinuity at the transition, and a shift of the transition temperature towards lower temperatures.

The evolution of lattice parameters of cubic phases have been fitted with straight lines, yielding the following thermal expansion  $\alpha_a$  coefficients: Cu100:  $7.1(3) \times 10^{-5} \text{ K}^{-1}$ ; Cu90:  $6.9(3) \times 10^{-5} \text{ K}^{-1}$ ; Cu82:  $7.1(3) \times 10^{-5} \text{ K}^{-1}$ ; Cu54:  $5.9(2) \times 10^{-5} \text{ K}^{-1}$ . The reported values are all very similar and in good agreement with values reported for most cubic spinels. Variations of the cubic reference parameters,  $a_0$ , for determination of spontaneous strains of the tetragonal phase were obtained by extrapolation to lower temperatures of these fits. The  $a$  and  $c$  parameters of the tetragonal phase do not

converge symmetrically into the extrapolated values of  $a_0$  for the cubic phase because of a volume expansion associated with the transition.

The temperature dependence of the angles within the  $(\text{Cu,Mg})\text{O}_4$  tetrahedron is illustrated in Fig. 6 for all the analysed Cu-rich samples. Heating results in a gradual reduction of the compression of the tetrahedron but, clearly, the compression remains significant until near the transition temperature. The variation with temperature of the O–(Cu,Mg)–O angles for the samples of intermediate composition mimics the change in the lattice parameters, the discontinuity of distortion at the transition decreases when Mg is added.

The nature of JT transitions, cooperative or order–disorder, at the solid state has been debated at length and both scenarios observed in several phases (for a review see,



Table 7

Selected geometrical parameters for  $\text{Mg}_{0.10}\text{Cu}_{0.90}\text{Cr}_2\text{O}_4$  (Cu90) at HT.

Standard deviations are in parentheses and refer to the last significant digits. OAV = Octahedral Angle Variance; OQE = Octahedral Quadratic Elongation; TAV = Tetrahedral Angle Variance; TQE = Tetrahedral Quadratic Elongation (Robinson *et al.*, 1971).

	298 K	373 K	473 K	573 K	673 K	773 K	873 K	973 K	1073 K	1173 K
$V_{\text{oct.}} (\text{\AA}^3)$	10.31	10.34	10.36	10.36	10.39	10.38	10.36	10.41	10.42	10.46
$\text{Cr}-\text{O}_{\text{axial}} (\text{\AA}) \times 2$	1.990 (4)	1.990 (6)	1.990 (7)	1.990 (6)	1.999 (6)	1.991 (2)	1.991 (3)	1.994 (3)	1.994 (3)	1.997 (3)
$\text{Cr}-\text{O}_{\text{eq.}} (\text{\AA}) \times 4$	1.986 (2)	1.989 (2)	1.990 (3)	1.990 (3)	1.989 (3)	1.991 (2)	1.991 (3)	1.994 (3)	1.994 (3)	1.997 (3)
$\text{Cr}-\text{O}_{\text{av.}} (\text{\AA})$	1.988	1.989	1.990	1.990	1.992	1.991 (2)	1.991 (3)	1.994 (3)	1.994 (3)	1.997 (3)
OAV ( $^\circ$ )	37.33	36.51	36.72	37.53	37.17	36.68	38.43	37.42	38.50	37.48
OQE	1.0101	1.0099	1.0099	1.0101	1.0100	1.0097	1.0102	1.0099	1.0102	1.0099
$\text{Cr}-\text{Cr} (\text{\AA})$	2.8914 (2)	2.8946 (1)	2.8995 (1)	2.9053 (2)	2.9130 (4)	2.9484 (2)	2.9503 (2)	2.9530 (2)	2.9557 (2)	2.9581 (2)
$V_{\text{tet.}} (\text{\AA}^3)$	3.74	3.75	3.78	3.82	3.85	3.96	3.99	3.99	4.01	4.01
$(\text{Cu,Mg})-\text{O} (\text{\AA})$	1.962 (3)	1.962 (4)	1.965 (5)	1.969 (5)	1.971 (4)	1.976 (5)	1.981 (6)	1.981 (6)	1.985 (6)	1.984 (7)
$\text{O}-(\text{Cu,Mg})-\text{O} (^\circ) \times 2$	103.8 (1)	104.0 (1)	104.3 (2)	104.6 (2)	105.0 (1)	109.47	109.47	109.47	109.47	109.47
$\text{O}-(\text{Cu,Mg})-\text{O} (^\circ) \times 4$	121.6 (2)	121.2 (3)	120.5 (4)	119.7 (3)	118.8 (3)	109.47	109.47	109.47	109.47	109.47
$\text{O}\cdots\text{O}$ edge ( $\text{\AA}) \times 2$	3.087	3.091	3.102	3.117	3.128	3.227	3.235	3.234	3.241	3.240
$\text{O}\cdots\text{O}$ edge ( $\text{\AA}) \times 4$	3.424	3.418	3.411	3.405	3.392	3.227	3.235	3.234	3.241	3.240
TAV ( $^\circ$ )	84.57	78.94	70.12	60.42	50.54	0	0	0	0	0
TQE	1.0234	1.0217	1.0192	1.0164	1.0136	1.0000	1.0000	1.0000	1.0000	1.0000

Table 8

Selected geometrical parameters for  $\text{Mg}_{0.18}\text{Cu}_{0.82}\text{Cr}_2\text{O}_4$  (Cu82) at HT.

Standard deviations are in parentheses and refer to the last significant digits. OAV = Octahedral Angle Variance; OQE = Octahedral Quadratic Elongation; TAV = Tetrahedral Angle Variance; TQE = Tetrahedral Quadratic Elongation (Robinson *et al.*, 1971).

	298 K	373 K	473 K	573 K	623 K	673 K	723 K	823 K	923 K	1023 K
$V_{\text{oct.}} (\text{\AA}^3)$	10.29	10.29	10.37	10.24	10.36	10.44	10.43	10.41	10.43	10.43
$\text{Cr}-\text{O}_{\text{axial}} (\text{\AA}) \times 2$	1.983 (7)	1.989 (8)	1.997 (7)	1.984 (8)	1.986 (7)	1.995 (7)	1.994 (3)	1.993 (3)	1.995 (3)	1.995 (3)
$\text{Cr}-\text{O}_{\text{eq.}} (\text{\AA}) \times 4$	1.987 (4)	1.985 (4)	1.988 (4)	1.984 (4)	1.993 (4)	1.995 (7)	1.994 (3)	1.993 (3)	1.995 (3)	1.995 (3)
$\text{Cr}-\text{O}_{\text{av.}} (\text{\AA})$	1.986	1.986	1.991	1.984	1.990	1.995 (7)	1.994 (3)	1.993 (3)	1.995 (3)	1.995 (3)
OAV ( $^\circ$ )	37.22	38.40	35.60	41.73	35.76	34.65	33.39	35.50	36.03	36.65
OQE	1.0100	1.0103	1.0096	1.0111	1.0095	1.0092	1.0089	1.0094	1.0095	1.0097
$\text{Cr}-\text{Cr} (\text{\AA})$	2.8958 (2)	2.8990 (2)	2.9041 (2)	2.9115 (2)	2.9165 (3)	2.950 (1)	2.9463 (2)	2.9493 (1)	2.9522 (2)	2.9538 (2)
$V_{\text{tet.}} (\text{\AA}^3)$	3.78	3.80	3.79	3.92	3.87	3.94	3.91	3.95	3.97	3.98
$(\text{Cu,Mg})-\text{O} (\text{\AA})$	1.963 (6)	1.967 (6)	1.962 (6)	1.980 (6)	1.968 (6)	1.973 (13)	1.967 (6)	1.974 (5)	1.977 (6)	1.979 (6)
$\text{O}-(\text{Cu,Mg})-\text{O} (^\circ) \times 2$	104.5 (2)	104.5 (2)	104.7 (2)	105.4 (2)	106.1 (2)	109.47	109.47	109.47	109.47	109.47
$\text{O}-(\text{Cu,Mg})-\text{O} (^\circ) \times 4$	120.1 (4)	120.0 (4)	119.6 (4)	117.9 (4)	116.5 (4)	109.47	109.47	109.47	109.47	109.47
$\text{O}\cdots\text{O}$ edge ( $\text{\AA}) \times 2$	3.104	3.110	3.107	3.151	3.145	3.221	3.212	3.224	3.229	3.233
$\text{O}\cdots\text{O}$ edge ( $\text{\AA}) \times 4$	3.402	3.408	3.392	3.391	3.348	3.221	3.212	3.224	3.229	3.233
TAV ( $^\circ$ )	64.95	64.79	59.14	41.07	29.37	0	0	0	0	0
TQE	1.0177	1.0177	1.0161	1.0110	1.0078	1.0000	1.0000	1.0000	1.0000	1.0000

*e.g.*, Kugel & Khomskii, 1982; Goodenough, 1998; Bersuker, 2006). Similarly, in copper spinel, two mechanisms for the JT transition can be proposed: in the first case, upon increasing  $T$ , all tetrahedra transform from flattened in the JT distorted spinel to ideal in the cubic spinel; in the second case, the energy-lowering cation coordination distortions persist above the structural transition temperature and  $\text{CuO}_4$  tetrahedra are always locally JT distorted. In the latter hypothesis, the structural transition has to be regarded as an order–disorder transition, at which local JT distortions become spatially uncorrelated, although do not disappear; the average crystal structure, which would in turn result in regular tetrahedra, accounts for this disorder through increased thermal displacement parameters.

In the case of JT transitions in systems with octahedrally coordinated cations, as in the case of manganite perovskites, large ADPs for O atoms are observed in the disordered phase along the cation–O bonds, reflecting the largest static bond length distribution (*i.e.* a mixture of long and short bonds) in

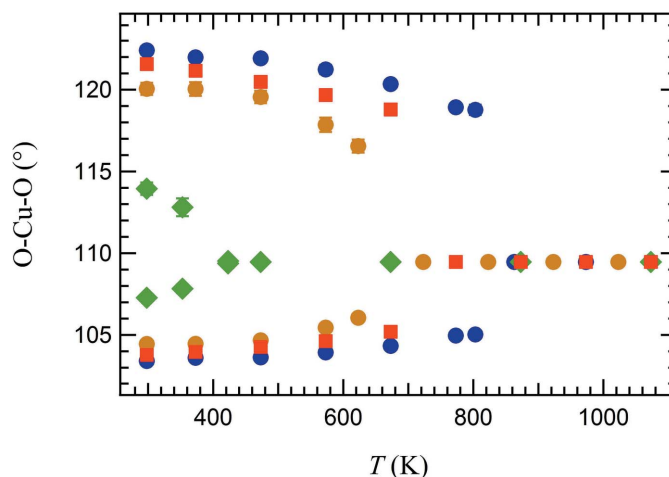


Figure 6 Variation of tetrahedral  $\text{O}-(\text{Cu,Mg})-\text{O}$  angles as a function of temperature. Blue:  $\text{CuCr}_2\text{O}_6$ ; red:  $\text{Mg}_{0.10}\text{Cu}_{0.90}\text{Cr}_2\text{O}_4$ ; orange:  $\text{Mg}_{0.18}\text{Cu}_{0.82}\text{Cr}_2\text{O}_4$ ; green:  $\text{Mg}_{0.46}\text{Cu}_{0.54}\text{Cr}_2\text{O}_4$ . Error bars are within the symbols.

**Table 9**

Selected geometrical parameters for  $\text{Mg}_{0.46}\text{Cu}_{0.54}\text{Cr}_2\text{O}_4$  [Cu54,  $x$  (EPMA) = 0.460(71)] at HT.

Standard deviations are in parentheses and refer to the last significant digits. OAV = Octahedral Angle Variance; OQE = Octahedral Quadratic Elongation; TAV = Tetrahedral Angle Variance; TOE = Tetrahedral Quadratic Elongation (Robinson *et al.*, 1971).

	298 K	353 K	473 K	673 K	873 K	1073 K	423 K†
$V_{\text{oct.}} (\text{Å}^3)$	10.23	10.32	10.38	10.47	10.45	10.59	10.45
$\text{Cr}-\text{O}_{\text{axial}} (\text{Å}) \times 2$	1.978 (7)	1.982 (10)	1.992 (3)	1.997 (3)	1.996 (3)	2.004 (3)	1.989 (5)
$\text{Cr}-\text{O}_{\text{eq.}} (\text{Å}) \times 4$	1.985 (5)	1.990 (6)	1.992 (3)	1.997 (3)	1.996 (3)	2.004 (3)	1.998 (3)
$\text{Cr}-\text{O}_{\text{av.}} (\text{Å})$	1.983	1.987	1.992 (3)	1.997 (3)	1.996 (3)	2.004 (3)	1.995
OAV ( $^\circ$ )	38.76	36.58	36.04	33.79	36.93	32.74	32.00
OQE	1.0103	1.0097	1.0095	1.0090	1.0098	1.0087	1.0085
$\text{Cr}-\text{Cr} (\text{Å})$	2.9212 (9)	2.929 (1)	2.9478 (8)	2.9514 (5)	2.9555 (6)	2.9600 (6)	2.945 (1)
$V_{\text{tet.}} (\text{Å}^3)$	3.92	3.92	3.95	3.93	3.99	3.95	3.89
$(\text{Cu,Mg})-\text{O} (\text{Å})$	1.973 (7)	1.971 (9)	1.974 (5)	1.972 (6)	1.981 (6)	1.975 (6)	1.964 (4)
$\text{O}-(\text{Cu,Mg})-\text{O} (^\circ) \times 2$	107.3 (2)	107.8 (3)	109.47	109.47	109.47	109.47	109.5 (1)
$\text{O}-(\text{Cu,Mg})-\text{O} (^\circ) \times 4$	114.0 (4)	112.8 (5)	109.47	109.47	109.47	109.47	109.4 (3)
$\text{O}\cdots\text{O}$ edge ( $\text{Å}$ ) $\times 2$	3.177	3.186	3.224	3.220	3.235	3.225	3.205
$\text{O}\cdots\text{O}$ edge ( $\text{Å}$ ) $\times 4$	3.308	3.284	3.224	3.220	3.235	3.225	3.208
TAV ( $^\circ$ )	11.86	6.60	0	0	0	0	0.01
TOE	1.0031	1.0017	1.0000	1.0000	1.0000	1.0000	1.0000

† On cooling.

**Table 10**

Selected geometrical parameters for  $\text{MgCr}_2\text{O}_4$  (Mg100) at HT.

Standard deviations are in parentheses and refer to the last significant digits.

	298 K	523 K	973 K
$V_{\text{oct.}} (\text{Å}^3)$	10.41	10.47	10.52
$\text{Cr}-\text{O} (\text{Å})$	1.993 (3)	1.996 (3)	2.000 (3)
OAV ( $^\circ$ )	33.93	33.10	35.71
OQE	1.0090	1.0088	1.0095
$\text{Cr}-\text{Cr} (\text{Å})$	2.9455 (1)	2.9493 (2)	2.9596 (2)
$V_{\text{tet.}} (\text{Å}^3)$	3.91	3.92	3.99
$\text{Mg}-\text{O} (\text{Å})$	1.968 (6)	1.969 (5)	1.981 (6)
$\text{O}\cdots\text{O}$ edge ( $\text{Å}$ )	3.214	3.215	3.236

these directions. In  $\text{CuCr}_2\text{O}_4$ , the distortions involve the tetrahedral angles, ADPs of Cu and O atoms are not elongated in a direction parallel to Cu–O bonds. ADPs of O atoms are elongated perpendicularly to the Cu–O bonds, whereas those of Cu atoms are elongated along the  $c$ -axis. Both these apparent vibrations affect the tetrahedral angles rather than bond lengths and may indicate the presence of disorder at the Cu sites in the tetragonal phase.

The temperature dependence of the isotropic atomic displacement parameters for Cu, Cr and O atoms in  $\text{CuCr}_2\text{O}_4$  and the intermediate compounds of the series  $\text{Mg}_x\text{Cu}_{1-x}\text{Cr}_2\text{O}_4$  is shown in Fig. 7. With increasing

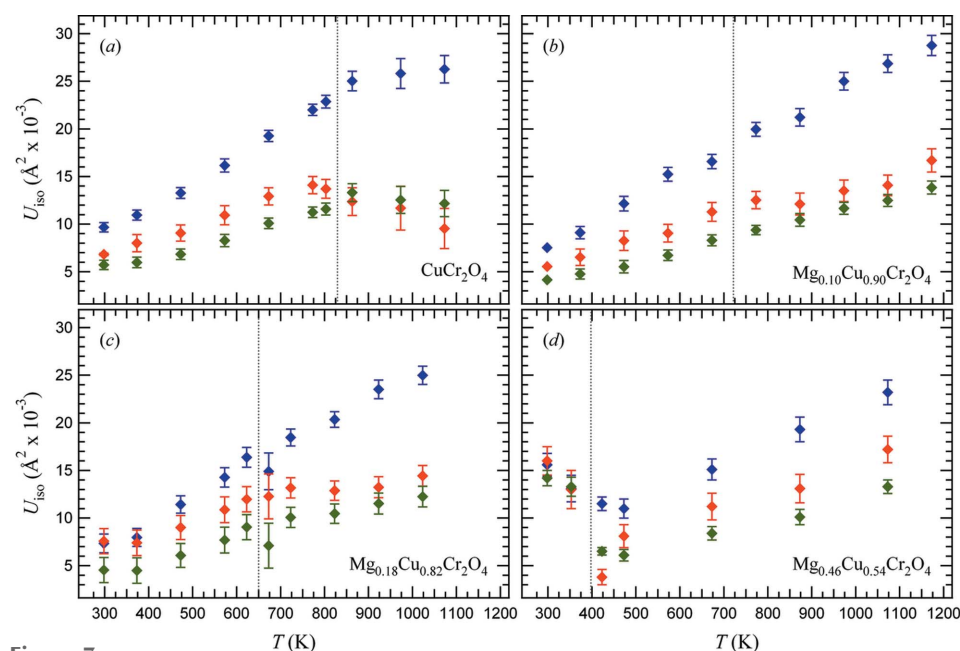


**Figure 7**

Variation as a function of temperature of isotropic atomic displacement parameters of Cu/Mg (blue diamonds), Cr (green diamonds) and O (red diamonds) atoms for spinel samples of different compositions across the  $\text{Mg}_x\text{Cu}_{1-x}\text{Cr}_2\text{O}_4$  join. (a)  $\text{CuCr}_2\text{O}_4$ ; (b)  $\text{Mg}_{0.10}\text{Cu}_{0.90}\text{Cr}_2\text{O}_4$ ; (c)  $\text{Mg}_{0.18}\text{Cu}_{0.82}\text{Cr}_2\text{O}_4$ ; (d)  $\text{Mg}_{0.46}\text{Cu}_{0.54}\text{Cr}_2\text{O}_4$ .

temperature up to the transition, the isotropic ADPs of the Cu-rich samples increase linearly, as expected within the harmonic approximation at  $T$  far from 0 K. All tetragonal datasets have linear extrapolation to 0 K that are negligible within  $3\sigma$ . This indicates the absence of a significant static disorder effect. In samples Cu90 and Cu82, this may be interpreted by considering that the ionic radii of both  $\text{Mg}^{2+}$  and  $\text{Cu}^{2+}$  in coordination 4 is 0.57 Å (Shannon, 1976). On the other hand, large scatter is displayed at low  $T$  by the ADPs of Cu54 sample, which shows a less clear trend in the tetragonal phase, likely due to compositional heterogeneities.

For all samples, a discontinuity in the temperature evolution of ADPs can be observed at the transition temperature. The observed behaviour of ADPs would suggest the

transition to be driven by cooperative distortion, although the presence of an order–disorder component cannot be excluded on the basis of average structure information only.

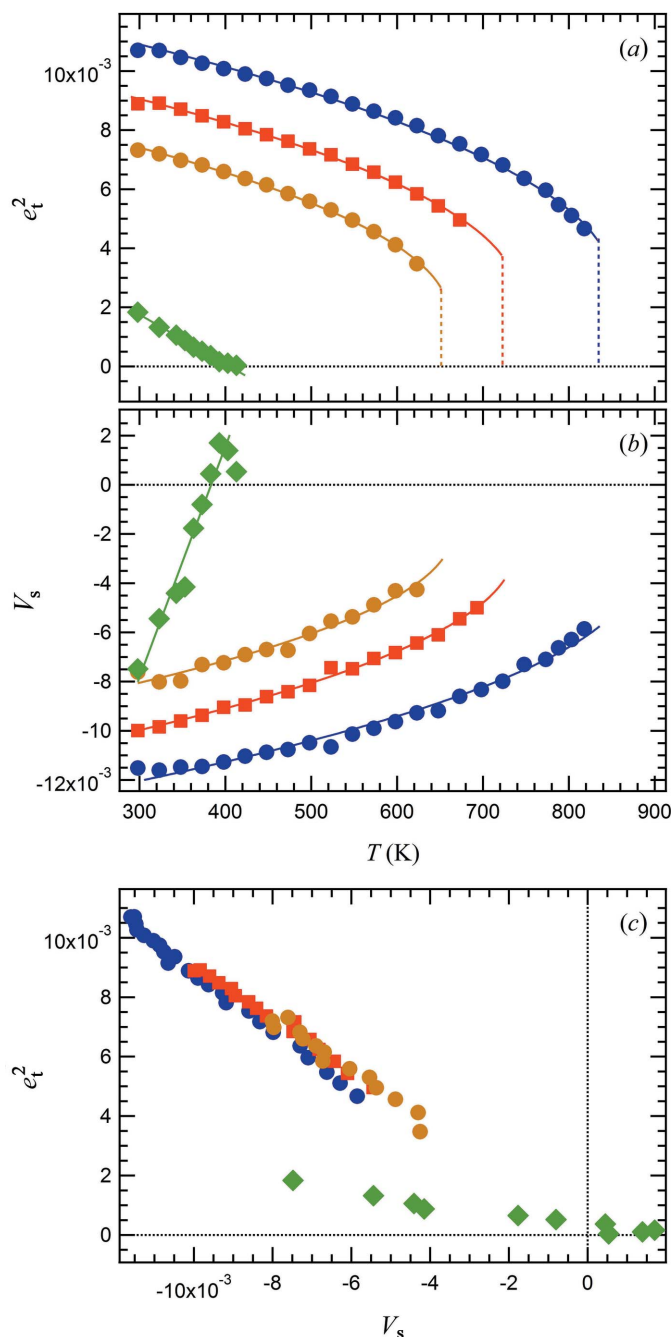


**Figure 8** Symmetry-adapted strains calculated from lattice parameters for Mg<sub>x</sub>Cu<sub>1-x</sub>Cr<sub>2</sub>O<sub>4</sub> with  $x = 0, 0.10, 0.18, 0.46$ . (a) The symmetry-adapted tetragonal strains follow the classical pattern of a first-order phase transition driven by a single-order parameter. (b) Volume strain,  $V_s$ , data have been fit with standard solutions to a Landau expansion assuming that  $V_s$  scales with the square of the order parameter. On this basis the transition is first order in character at  $x = 0, 0.10, 0.18$  and second order at  $x = 0.46$ . (c) Strain–strain relationships: tetragonal strains and volume strains vary linearly with each other at each composition and, within experimental uncertainty, extrapolate to the origin. Same symbols as for Fig. 6.

### 3.3. Spontaneous strain in CuCr<sub>2</sub>O<sub>4</sub>

Instability of the electronic structure is the driving mechanism for a Jahn–Teller transition. However, the change in the structural state appears overtly as changes in lattice parameters, and these can be described formally in terms of macroscopic strains. Variations of spontaneous strains accompanying a phase transition can be used to quantify the associated order parameters and are expected to provide detailed insights into the mechanisms of the transition itself. Strain parameters have been calculated by using the equations given by Carpenter, Salje & Graeme-Barber (1998), who reviewed the use of spontaneous strain to measure order parameters associated with phase transitions in minerals. In this case, there are two strains, the symmetry-breaking tetragonal shear strain,  $e_t = (1/\sqrt{3})(2e_3 - e_1 - e_2)$ , where  $e_2 = e_1 = (a - a_0)/a_0$ ,  $e_3 = (c - a_0)/a_0$ , and the volume strain,  $V_s = (V - V_0)/V_0$ .

Values for the reference parameter,  $V_0$ , were obtained by fitting a straight line to data for the unit-cell volume above the transition and extrapolating to lower temperatures. The resulting strains  $e_t^2$  and  $V_s$  are reported in Figs. 8(a) and 8(b) as a function of  $T$ .

Symmetry rules determine the nature of coupling between the strain and order parameters. The order parameter  $q_{JT}$  and the tetragonal strain  $e_t$  transform as  $\Gamma_3^+$  of  $Fd\bar{3}m$ , the active representation for the transition to  $I4_1/amd$ , giving coupling of the form  $\lambda e_t q_{JT}$ .  $V_s$ , which does not break the cubic symmetry of the high-temperature phase, transforms as the identity representation and is proportional to  $q_{JT}^2$ . Therefore, the expected relationships between strain components are:  $e_t \propto V^{1/2} \propto q_{JT}$ . Two strains show a linear dependence when plotted as  $e_t^2$  versus  $V_s$  (Fig. 8c), consistent with these symmetry considerations.

The simultaneous linear and quadratic coupling of strain components to the Jahn–Teller order parameter implies a renormalization of the Landau expansion in order parameter for free energy (Landau & Lifshitz, 1958): the transition temperature is renormalized by coupling between the Jahn–Teller order parameter and the symmetry-breaking strain  $e_t$ , while the fourth-order term of the expansion contains contributions from coupling of the square of  $q_{JT}$  with the volume strain.

With increasing Mg content, the magnitudes of the strains all decrease (Figs. 8a and 8b). A decrease in the discontinuity at the transition and a trend towards linear behaviour are also fairly evident.

The  $Fd\bar{3}m \leftrightarrow I4_1/amd$  transition is required to be first order in character due to the existence of a third-order term in  $q_{JT}$ . However, the strain variations with temperatures are not well represented by the standard solution for the order parameter

$$q_{JT} = \frac{3}{4} q_{0,JT} \left\{ 1 + \left[ 1 - \frac{4}{9} \frac{T - T_c^*}{T_{tr} - T_c^*} \right]^{1/2} \right\},$$

where  $T_{tr}$  is the transition temperature and  $T_c^*$  the renormalized critical temperature. Rather, the data for Cu100, Cu90

and Cu82 are well represented by the standard solution for a 246 solution with negative fourth-order coefficient (reported here, from Carpenter, Salje, Graeme-Barber, Wruck *et al.*, 1998)

$$q_{JT}^2 = \frac{3}{2} q_{0,JT}^2 \left\{ 1 + \left[ 1 - \frac{3}{4} \frac{T - T_c^*}{T_{tr} - T_c^*} \right]^{1/2} \right\}$$

as shown in Figs. 8(a) and (b). At  $T = T_{tr}$ , the jump in the value of  $q_{JT}$  from zero to  $q_{0,JT}$  is

$$q_{0,JT}^2 = -\frac{4a}{b^*} (T_{tr} - T_c^*),$$

where  $a$  and  $b^*$  here are the second- and the renormalized fourth-order terms in the Landau expansion, respectively.

The equilibrium transition temperature  $T_{tr}$  for the three Cu-rich samples, as determined by  $e_1^2$  fits reported in Fig. 8, is 834 K ( $T_c^*$  set to 780 K and  $q_{0,JT}^2 = 4.34 \times 10^{-3}$ ) for Cu100, 722 K ( $T_c^*$  set to 675 K and  $q_{0,JT}^2 = 3.76 \times 10^{-3}$ ) for Cu90, and 651 K ( $T_c^*$  set to 625 K and  $q_{0,JT}^2 = 2.65 \times 10^{-3}$ ) for Cu82.  $T_{tr}$  decreases linearly as a function of  $X_{Mg}$  as evident in Fig. 9, where the transition temperature for  $MgCr_2O_4$  (data from Kemei *et al.*, 2013) is also shown for comparison. The difference between  $T_{tr}$  and  $T_c^*$ , which is a measure of the extent of the first-order character of the transition, decreases systematically with increasing Mg content as well.

At  $x = 0.46$ , the transition conforms to  $V_s \propto e_1^2 \propto q_{JT}^2 \propto (T_c^* - T)$ , with  $T_c^* = 407$  K, and thus appears to be second order in character.

This is all consistent with the third-order term being small for the Cu–Mg spinel system and the change from first-order to second-order character being due to changes in the value of the fourth-order coefficient. Coupling of the volume strain with the order parameter leads to a renormalization of the fourth-order coefficient and reductions in the strength of this coupling, as appears to occur with increasing Mg content, would contribute to this trend.

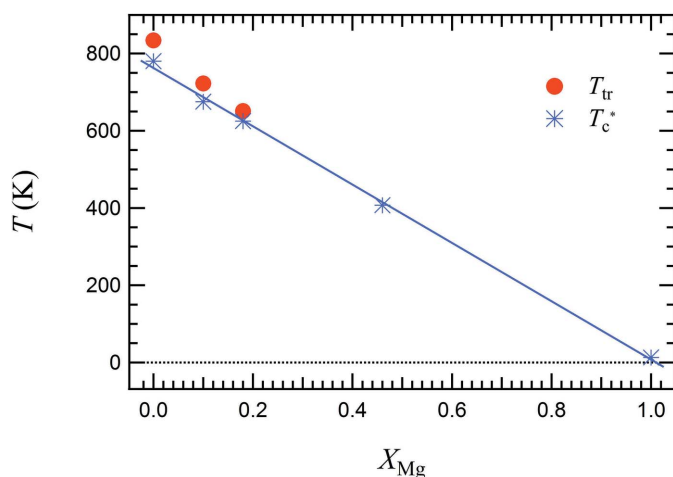


**Figure 9**  
Variation of  $T_{tr}$  and  $T_c^*$  as a function of Mg content. Magnetic driven structural transition temperature (Néel temperature) for  $MgCr_2O_4$  (Kemei *et al.*, 2013) is also shown for comparison.

#### 4. Summary

Tetragonal distortion of Cu-rich members of the  $Mg_xCu_{1-x}Cr_2O_4$  spinel solid solution, due to a cooperative Jahn–Teller effect, can be suppressed either by increasing temperature or by gradually replacing  $Cu^{2+}$  with  $Mg^{2+}$ . The effect is to dilute the nearest-neighbour interactions of  $Cu^{2+}$  ions, thus reducing the efficiency of the cooperative distortion. With increasing the Mg content, a gradual reduction of the splitting of  $a$  and  $c$  unit-cell parameters and of the flattening of the tetrahedra is observed, and the transition temperature also decreases.

Jahn–Teller distortions of individual (Mg,Cu) tetrahedra are accompanied by variations in unit-cell parameters. Large spontaneous strains, coupling with an order parameter which originates physically from an electronic instability, lead to mean-field behaviour. The underlying role of strain in promoting long-range interactions is confirmed by the analysis of strain evolution, which shows that the Jahn–Teller phase transitions in  $CuCr_2O_4$  conform to mean-field behaviour. Increasing Mg content causes reductions in the magnitude of the strains, and the two coupling coefficients also reduce with increasing Mg content. Reducing the coupling with the volume strain reduces in turn the renormalization of the fourth-term order Landau coefficient so that it goes from negative to positive, hence the tetragonal-to-cubic phase transition evolves from first order for Cu-rich samples towards second order at an intermediate composition.

#### Acknowledgements

The authors thank Professor Paolo Ghigna (University of Pavia, Italy) for his help with the synthesis of some compounds. The Bayerisches Geoinstitut (University of Bayreuth, Germany) and Mr Detlef Krause are acknowledged for making microprobe time available and for helping with the analyses.

#### References

- Aizu, K. (1969). *J. Phys. Soc. Jpn*, **27**, 387–396.
- Atanasov, M., Kesper, U., Ramakrishna, B. & Reinen, D. (1993). *J. Solid State Chem.* **105**, 1–18.
- Bersuker, B. I. (2006). *The Jahn–Teller Effect*, pp. 1–616. Cambridge University Press.
- Blessing, R. H. (1995). *Acta Cryst.* **A51**, 33–38.
- Blessing, R. H., Coppens, P. & Becker, P. (1974). *J. Appl. Cryst.* **7**, 488–492.
- Carpenter, M. A., Salje, E. K. H. & Graeme-Barber, A. (1998). *Eur. J. Mineral.* **10**, 621–691.
- Carpenter, M. A., Salje, E. K. H., Graeme-Barber, A., Wruck, B., Dove, M. T. & Knight, K. S. (1998). *Am. Mineral.* **83**, 2–22.
- Crottaz, O., Kubel, F. & Schmid, H. (1997). *J. Mater. Chem.* **7**, 143–146.
- De, K. S., Ghose, J. & Murthy, S. R. C. (1983). *J. Solid State Chem.* **47**, 264–277.
- Goodenough, J. (1998). *Annu. Rev. Mater. Sci.* **28**, 1–27.
- Ibers, J. A. & Hamilton, W. C. (1974). *International Tables for X-ray Crystallography*, Vol. 4, pp. 99–101. Birmingham, UK: Kynoch Press.

- Kemei, M. C., Barton, P. T., Moffitt, S. L., Gaultois, M. W., Kurzman, J. A., Seshadri, R., Suchomel, M. R. & Kim, Y.-I. (2013). *J. Phys. Condens. Matter*, **25**, 326001.
- Kennedy, B. & Zhou, Q. (2008). *J. Solid State Chem.* **181**, 2227–2230.
- Kugel, K. I. & Khomskii, D. I. (1982). *Sov. Phys. Usp.* **25**, 231–256.
- Landau, L. D. & Lifshitz, E. M. (1958). *Statistical Physics*. Reading, Massachusetts: Addison Wesley.
- Lehmann, M. S. & Larsen, F. K. (1974). *Acta Cryst.* **A30**, 580–584.
- Lenaz, D., Skogby, H., Princivalle, F. & Hålenius, U. (2004). *Phys. Chem. Miner.* **31**, 633–642.
- North, A. C. T., Phillips, D. C. & Mathews, F. S. (1968). *Acta Cryst.* **A24**, 351–359.
- Reinen, D., Atanasov, M., Nikolov, G. & Steffens, F. (1988). *Inorg. Chem.* **27**, 1678–1686.
- Robinson, K., Gibbs, G. V. & Ribbe, P. H. (1971). *Science*, **172**, 567–570.
- Shannon, R. D. (1976). *Acta Cryst.* **A32**, 751–767.
- Sheldrick, G. M. (2008). *Acta Cryst.* **A64**, 112–122.
- Sheldrick, G. M. (2003). *SADABS*. University of Göttingen, Germany.
- Shoemaker, D. P. & Seshadri, R. (2010). *Phys. Rev. B*, **82**, 214107.
- Yé, Z., Crottaz, O., Vaudano, F., Kubel, F., Tissot, P. & Schmid, H. (1994). *Ferroelectrics*, **162**, 103–118.